4-4　光–マイクロ波リンクと TAI 校正
4-4　TAI Calibration with an Optical Standard

Nils Nemitz　蜂須英和　中川史丸　伊東宏之　後藤忠広　井戸哲也
Nils NEMITZ, Hidekazu HACHISU, Fumimaru NAKAGAWA, Hiroyuki ITO, Tadahiro GOTOH, and Tetsuya IDO

近い将来に実施が見込まれている秒の再定義を見据えて、光原子時計がローカルあるいはグローバルな時系生成へ寄与し始めている。NICT で開発しているストロンチウム光格子時計 NICT-Sr1 は、国際的な標準時系のひとつである国際原子時（TAI）の直近の歩度校正に初めて寄与した光原子時計の一つである。本稿では、NICT-Sr1 による TAI 校正の実施と、長距離遠隔評価における不確かさについて議論する。

In anticipation of a future redefinition of the SI second, atomic clocks based on optical transitions are now contributing to the generation of local and global time scales. The strontium optical lattice clock NICT-Sr1 is one of two such clocks that first actively contributed to the steering of the international time scale TAI. Here we discuss the implementation and uncertainty budget for such a long-distance remote evaluation of the time scale by a frequency standard in the optical domain.

1 Introduction

In our daily lives, we typically interact with a local time that is derived from Coordinated Universal Time (UTC) by applying a fixed offset, such as +9 hours in the case of Japan Standard Time. But UTC itself, maintained by the International Bureau for Weights and Measures (BIPM), similarly relies on two underlying time scales [1]: At the lowest level, a weighted mean over more than 350 precision clocks at institutes throughout the world is used to realize the free atomic time scale EAL (Échelle Atomique Libre). While the result is highly stable, its accuracy is limited by the residual frequency errors of the contributing clocks.

International Atomic Time (TAI) corrects for these errors to implement a scale interval that accurately represents the SI second, before an integer number of leap seconds is added to create UTC, which maintains synchronization with Earth's rotation.

The continued calibration of TAI is performed by purpose-built frequency standards. For those directly implementing the SI definition of the second based on the 9.192 GHz microwave transition in ^{133}Cs, systematic uncertainties approach 1 part in 10^{16} [2]-[6]. In recent years optical frequency standards have improved rapidly, and the laboratories that maintain Cs-based clocks now also operate frequency standards that interrogate atomic transitions in the optical regime with significantly lower uncertainties [7]-[13]. In a coordinated measurement performed in December 2018, SYRTE and NICT became the first institutes to contribute to the steering of TAI with such optical clocks.

An accurately calibrated international time scale has direct scientific value for applications such as long-term studies of pulsar timing [14]. It is also a prerequisite for improved agreement between local implementations [15]-[18], where it affects a wide range of applications from satellite navigation to stock trading.

2 Radio-frequency link

As shown in Fig.1, the junction point of such a measurement is a hydrogen maser (HM) that is continuously compared to TAI, while its radio frequency signals can simultaneously be evaluated by the strontium optical lattice clock NICT-Sr1.

This maser is part of the Japan Standard Time System [19], as described in Section **3-1** of this publication. As such, it is compared to the locally generated UTC(NICT) signal by a dual-mixer time difference (DMTD) system [20], which records data once per second. The time difference of UTC(NICT) relative to UTC, as implemented by BIPM is continuously evaluated using a GPS-PPP link [21].

The statistical uncertainty of the timing link is reported monthly in BIPM's Circular T [22]. In the following, we will adopt a representative value of $u_A(\mathrm{NICT}) = 0.35$ ns.

Since TAI and UTC differ only by a constant time offset, the satellite link allows the maser frequency to be evaluated in terms of the TAI scale interval. This frequency is typically expressed as the mean fractional deviation from nominal frequency $\bar{y}(\mathrm{HM})$ over the evaluated period T. The uncertainty of the link to TAI is given as [23]

$$u_{l/\mathrm{Tai}} = \frac{\sqrt{2}\,u_A(\mathrm{NICT})}{T_0} \Big/ \left(\frac{T}{T_0}\right)^x \qquad (1)$$

with an exponent $x = 0.9$ in consideration of a measurement instability that largely results from (flicker) phase noise. $T_0 = 5$ d represents the reporting interval of the Circular T. For $T = 35$ d, the link uncertainty results in a fractional frequency uncertainty $u_{l/\mathrm{Tai}} = 2.0 \times 10^{-16}$. The uncertainty contribution from the DMTD system is insignificant in comparison [20].

3 RF-to-optical comparison

An additional 100 MHz signal is transferred from the hydrogen maser to the optical clock laboratory, where it is converted to 9.2 GHz by a phase-locked dielectric resonator oscillator (DRO) with additive noise of −114 dBc/Hz at 1 kHz separation from the carrier.

NICT-Sr1 provides an optical signal at ν_{clk} that is continuously steered to represent the Sr clock transition frequency of $\nu_{Sr} \approx 429$ THz. It differs from this only through a fixed frequency offset $\delta\nu_{\mathrm{prb}} = 80$ MHz that allows an acousto-optic modulator to probe the atomic spectrum without affecting ν_{clk} and by the carefully evaluated systematic shift $\delta\nu_{\mathrm{sys}}$ of the transition frequency through physical effects (discussed in Section **4-3**). Although NICT-Sr1 only interrogates the atomic transition for 80 ms every 1.75 s, the ultra-stable cavity used for the optical local oscillator allows for the generation of a phase-continuous signal with a stability characterized by an Allan deviation of $\sigma_y(\tau) = 7 \times 10^{-15}\,(\tau/\mathrm{s})^{-1/2}$ [24].

An optical frequency comb based on ytterbium-doped optical fiber (Menlo Systems Orange Comb) is used for down-conversion from the optical to the radio-frequency domain. The carrier-envelope offset frequency f_{CEO} is phase-locked to an external reference, and the repetition rate is stabilized to maintain a constant phase of the beat

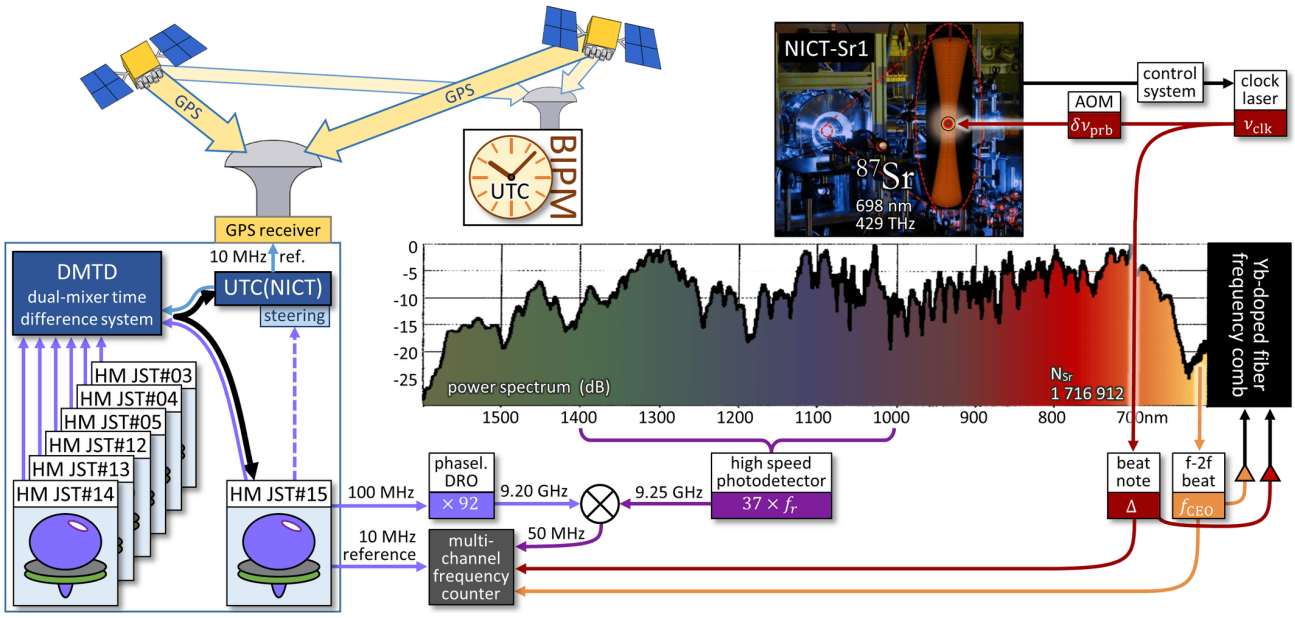

Fig. 1 Overview of the TAI calibration scheme
A hydrogen maser forms the junction point that is simultaneously evaluated in relation to the strontium optical lattice clock NICT-Sr1 and UTC(NICT). Although the presently evaluated maser (HM JST#15) also serves as source clock for UTC(NICT), these roles can be assigned to any combination of masers as long as DMTD comparison data is available. The link to UTC, and thus TAI, is realized through a GPS receiver referenced to UTC(NICT). NICT-Sr1 provides a laser at $\nu_{\mathrm{clk}} \approx 429$ THz that is continuously steered to the atomic clock transition. A fixed frequency offset of $\delta\nu_{\mathrm{prb}} = 80$ MHz allows the shape of the atomic spectrum to be probed by an acousto-optic modulator (AOM) without disturbing ν_{clk}. An optical frequency comb based on Yb-doped fiber is stabilized to the clock laser. A multiple of the comb repetition rate f_r is then down-mixed with a multiple of the reference maser frequency generated by a phase-locked dielectric resonator oscillator (DRO). The resulting frequency of approximately 50 MHz is counted on a zero-dead-time multichannel frequency counter, together with the beat note Δ of the comb with the clock laser, and the beat signal used to stabilize the carrier-envelope offset frequency f_{CEO}. The latter two provide diagnostic information.

signal $\Delta = \nu_n - \nu_{\mathrm{clk}}$ generated by the clock laser and the nearest comb line with index $n = 1\,716\,912$. Two channels of a zero-dead-time counter (K+K Messtechnik FXE) are dedicated to monitoring f_{CEO} and Δ. The measurements show fractional uncertainty contributions from $f_{\mathrm{CEO}}/\nu_{Sr}$ and Δ/ν_{Sr} to be close to 1×10^{-16} at 1 s averaging time. Since

$$\nu_{Sr} + \delta\nu_{\mathrm{sys}} = f_{\mathrm{CEO}} + n\, f_r + \Delta + \delta\nu_{\mathrm{prb}}, \tag{2}$$

the comb repetition rate f_r then reproduces the optical clock's stability. It is detected by a photo-detector (Discovery Semiconductors DSC40S) with a 3 dB bandwidth of 15.6 GHz, using the comb output spectrum >1000 nm extracted by a dichroic mirror. The resulting radio-frequency signal consists of a series of harmonics of the repetition rate, with more than 60 dB signal-to-noise ratio (at 300 kHz RBW) up to 10 GHz. Adjusted for measurement bandwidth and considering only white phase noise, this corresponds to a power spectral density (PSD) of $\mathcal{L} = -110$ dBc/Hz.

The repetition rate signal is down-mixed with the 9.2 GHz signal derived from the hydrogen maser, and the resulting component at $f_{dm} = 50$ MHz is amplified to 13 dBm for detection. The output signal shows a phase noise level equivalent to $\mathcal{L} = -90$ dBc/Hz.

The corresponding single sided fractional frequency PSD

$$S_y(f) = \left(\frac{f}{f_0}\right)^2 \cdot 2 \cdot 10^{\frac{\mathcal{L}(f)}{10}} = 2 \times 10^{-9} \left(\frac{f}{f_0}\right)^2, \tag{3}$$

allows the resulting stability limit for an investigated signal frequency f_0 to be calculated as an Allan variance

$$\sigma_y^2(\tau) = 2 \int_0^{f_H} S_y(f) \frac{(\sin \pi\tau f)^4}{(\pi\, \tau\, f)^2} df\,. \tag{4}$$

For a detection bandwidth of $f_H = 2.5$ MHz realized by a tunable cavity filter, this yields $\sigma_y(\tau) = 0.019 \cdot (\tau\, f_0)^{-1}$. For detection at the fundamental of the repetition rate $f_0 = f_r = 250$ MHz, this would give $\sigma_y(1s) = 7.8 \times 10^{-11}$. However, by detecting the repetition rate at a harmonic $n_r = 37$, the increased $f_0 = 37 \cdot 250$ MHz $= 9\,250$ MHz reduces this to $\sigma_y(1s) = 2.1 \times 10^{-12}$. The frequency is measured on the third channel of the dead-time free frequency counter. The counter samples the phase every ms and averages the results over a 1 s sampling window to further reduce the phase-noise induced instability.

The synchronous measurements of Δ and f_{CEO}, both of which show instabilities of < 50 mHz at 1 s averaging time, clearly indicate any cycle slips in the stabilization of the frequency comb, which typically result from disturbances of the clock laser frequency. By referencing the frequency counter to a 10 MHz signal provided by the maser, the measurement of the clock laser frequency then includes the frequency deviation y_{HM} of the hydrogen maser as

$$\left[f_{\mathrm{CEO}} + \frac{n_{Sr}}{n_r}(9.2\ \mathrm{GHz} + f_{dm})\, f_r + \Delta\right]/(1 + y_{\mathrm{HM}}) \tag{5}$$
$$= \nu_{Sr} + \delta\nu_{\mathrm{sys}}.$$

Combined with $\nu_{Sr} = 429\,228\,004\,229\,873.00(17)$ Hz as recommended by the International Committee for Weights and Measures (CIPM) for ^{87}Sr as a secondary representation of the second in 2017 [25], this directly yields y_{HM}.

4 Measurement stability

The instability of y_{HM} and relevant contributions are shown in Fig.2 in terms of the fractional overlapping Allan deviation. For $\tau < 10$ s we observe an initial slope $\sigma_y(\tau) \approx 1 \times 10^{-13}(\tau/1\ \mathrm{s})^{-1}$, representing a dominant phase noise contribution. We find this noise to be largely common-mode between the described frequency measurement system and a separate system detecting the fourth harmonic of the repetition rate, and expect that it represents noise either present on the maser signal itself, or introduced in the transfer to the frequency comb laboratory.

Over the interval from 10 s to 10^4 s, the Allan deviation is best described by $\sigma_y(\tau) = 3.4 \times 10^{-16}\ (\tau/10^4\ \mathrm{s})^{-0.53}$, with a slope close to the expectation for white frequency noise (WFN). We extrapolate this contribution according to $(\tau/10^4\ \mathrm{s})^{-0.5}$ to find a statistical uncertainty $u_{\mathrm{sta}} = 3.9 \times 10^{-17}$ for $\tau = 779\,853$ s representing the total available data obtained during a 10 d measurement campaign.

At the observed instability, a more convenient averaging time of 16 h ($\tau = 57\,600$ s) is sufficient to characterize the maser frequency to a statistical uncertainty of $u_{\mathrm{sta}} = 1.4 \times 10^{-16}$, well below the limit of 2.0×10^{-16} set by the GPS link even for a 35 d evaluation period.

In the following, we will show that such limited measurement times suffice to compare NICT-Sr1 to TAI with an uncertainty of 3×10^{-16}, on par with the uncertainties reported by the best cesium fountains, and sufficient to test the recommended frequency of ^{87}Sr as a secondary representation of the second beyond its stated uncertainty of $u_{\mathrm{Srep}} = 4 \times 10^{-16}$.

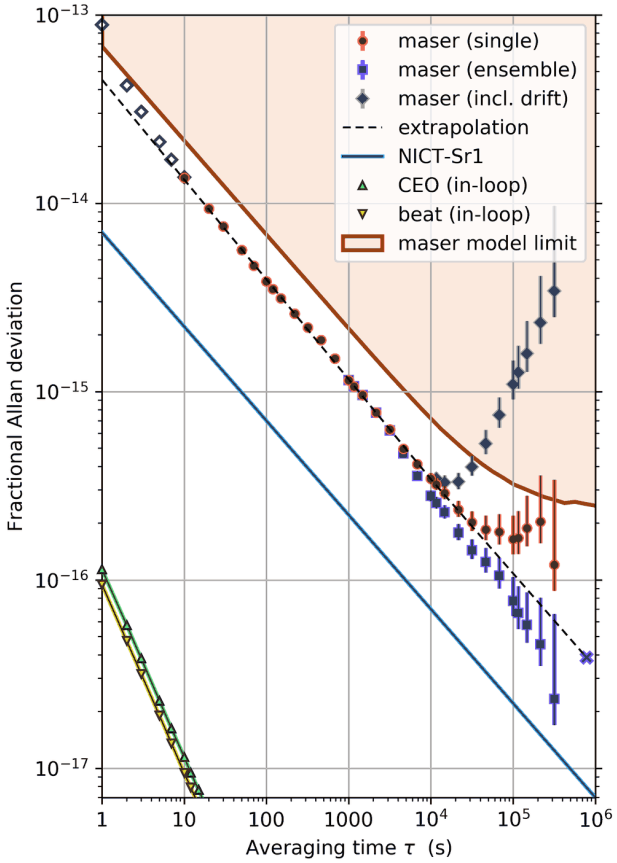

Fig. 2 Stability of a maser frequency evaluation over a 10 d period The linear drift of the maser leads to an increasing Allan deviation for averaging times t > 10^4 s (gray solid diamonds). After subtraction of a linear trend, the instability reaches a plateau near 2×10^{-16}, representing the maser flicker noise floor (red circles). Correcting for non-linear drift based on an ensemble of 5 masers further reduces the observed instability (blue squares). The contributions from NICT-Sr1 (solid blue line) and the phase lock of the frequency comb's carrier-envelope offset and repetition rate (open triangles) do not significantly contribute to the measurement instability. Open diamonds indicate a subset of data evaluated at a time step of 1 s, where an initial slope of $\sigma_y(\tau) = 1 \times 10^{-13}/\tau$ indicates a significant phase noise contribution. The brown line represents the maser noise model discussed later in the text, with (drift-corrected) instabilities in the shaded region indicating instability above expectation.

5 Intermittent maser evaluation

The reporting interval used by BIPM consists of five-day periods that begin at UTC 0:00:00 for modified Julian dates (MJD) ending in 4 or 9. However, any measurement that spans only one or two such periods is likely to be limited by the timing uncertainty of the satellite link to BIPM. As described in Section **2**, the link used by NICT is characterized by a frequency uncertainty $u_{l/\mathrm{Tai}} = 2.0 \times 10^{-16}$ over $T = 35$ d. For $T = 10$ d, this is degraded to $u_{l/\mathrm{Tai}} = 6.1 \times 10^{-16}$.

As originally discussed in Ref. [24], the maser characterization does not require continuous operation of the optical clock, as the maser stability is sufficient to act as a flywheel oscillator between measurements. We consider the maser frequency fluctuations $\delta y(t)$ after removal of a persistent linear drift to represent stationary stochastic processes. Following the approach discussed in the supplement of Ref. [15], the average frequency over an arbitrary distribution of observation time can then be written as

$$\bar{y}_x = \int_{-\infty}^{\infty} y(t)\ g_x(t)\, dt, \tag{6}$$

with normalized weighting function

$$g_x(t) = \begin{cases} 1/T_x & \text{during measurement intervals} \\ 0 & \text{elsewhere} \end{cases} \tag{7}$$

Here T_x is the combined averaging time. The placeholder x refers to either the sampled intervals ($x \to s$) or the full evaluation period ($x \to p$). The frequency average over the sampled intervals $\bar{y}_s$ then deviates from the true average $\bar{y}_p$ by $\delta y = \bar{y}_s - \bar{y}_p$. The expectation value of δy is zero, and we consider the variance $u_{\mathrm{stc}}^2 = \langle \delta y^2 \rangle$ to represent the uncertainty u_{stc} due to unobserved stochastic behavior during measurement dead times. This relates directly to the power spectral density (PSD) $S_y(f)$ describing the maser frequency noise:

$$u_{\mathrm{stc}}^2 = \int_0^{\infty} S_y(f)\, |G_\Delta(f)|^2\, df\,. \tag{8}$$

Here $G_\Delta(f)$ is the Fourier transform of the differential weighting function $g_\Delta(t) = g_s(t) - g_p(t)$. Straightforward application of Parseval's theorem then immediately confirms two expectations: The first is that better agreement of $g_s(t)$ and $g_p(t)$, which reduces the integral over $g_\Delta(t)^2$, likewise reduces $|G_\Delta(f)|^2$, and therefore (generally) u_{stc}^2. The second is that for white frequency noise, where $S_y(f) = \mathrm{const}$, only the integral over the squared sensitivity function $|G_\Delta(f)|^2$ (and thus $g_\Delta(t)^2$) is relevant, while the distribution of sampling time is not. For the typical case of $T_s \ll T_p$, it is therefore sufficient to handle the white frequency noise contribution based on the observed Allan deviation as discussed in the previous section.

We extract the typical maser stability based on frequency differences recorded by the DMTD system. Using data from more than two years of simultaneous operation for four masers (HMJST#03, HMJST#12, HMJST#13, and HMJST#15), we average the Hadamard variances to extract a representative single-HM instability shown in Fig.3. We interpret this as a combination of white frequency noise (WFN), flicker frequency noise (FFN), and flicker-walk frequency modulation noise (FWFM) and we fit the data according to

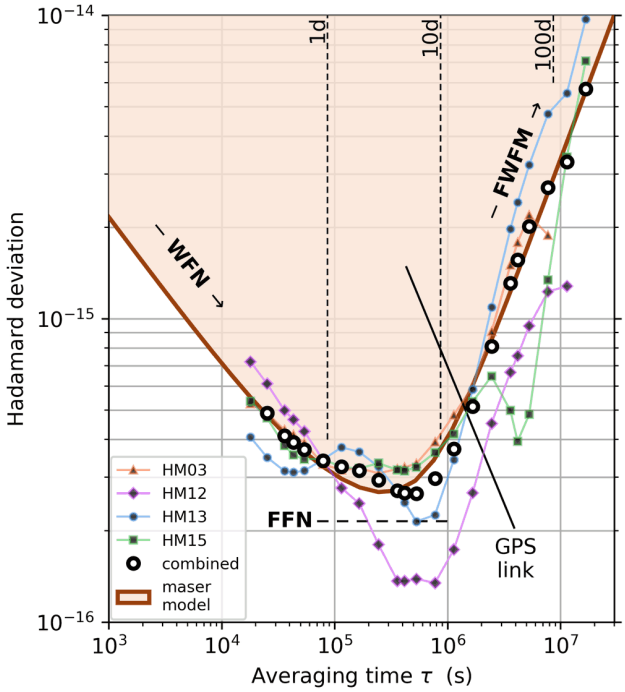

Fig. 3 Representative maser stability
Colored marks and guides show individual Hadamard deviations σ_H extracted from continuous DMTD data using a four-corner-hat method [26]. Heavy open circles represent the mean variance of maser-to-maser frequency differences. The thick solid line and shaded area represent the fitted maser model included in Fig.2 and Fig.5, which includes instabilities from white frequency noise (WFN), flicker frequency noise (FFN) and flicker-walk frequency modulation noise (FWFM). For averaging times $\tau > 16$ d the maser instability exceeds that of the GPS link (thin solid line). The plotted data includes a correction for $\sigma_H > u_{l/\mathrm{Tai}}$ [23].

$$\sigma_H^2(\tau) = \underbrace{a_{-1}^2\,(\tau/\mathrm{s})^{-1}}_{\mathrm{WFN}} + \underbrace{a_0^2}_{\mathrm{FFN}} + \underbrace{a_2^2\,(\tau/\mathrm{s})^2}_{\mathrm{FWFM}}. \tag{9}$$

We find coefficients $a_{-1} = 6.8 \times 10^{-14}$, $a_0 = 2.2 \times 10^{-16}$ and $a_2 = 3.4 \times 10^{-22}$. These relate [26] [27] to a PSD of

$$S_y(f) = \underbrace{h_0}_{\mathrm{WFN}} + \underbrace{h_{-1}/f}_{\mathrm{FFN}} + \underbrace{h_{-2}/f^3}_{\mathrm{FWFM}} \tag{10}$$

with coefficients $h_0 = 9.3 \times 10^{-27}\mathrm{Hz}^{-1}$, $h_{-1} = 4.1 \times 10^{-32}$ and $h_{-2} = 9.1 \times 10^{-45}\ \mathrm{Hz}^2$, calculated as elaborated in the appendix. By taking the discrete Fourier transform of $g_\Delta(t)$, u_{stc} can now be calculated for an arbitrary distribution of measurement time. Although the method is generally robust, the h_{-2}/f^3 term representing FWFM varies rapidly for near-zero frequencies. The numerical evaluation of eq.(8) is more consistent if the frequency resolution of the discrete Fourier transform is increased by zero-padding $g_\Delta(t)$. We then find agreement to better than 10% with a statistical analysis using Monte Carlo methods. For this, we generate random noise series according to the PSD coefficients using the method described in Ref. [28].

Within this framework, we can now investigate effective

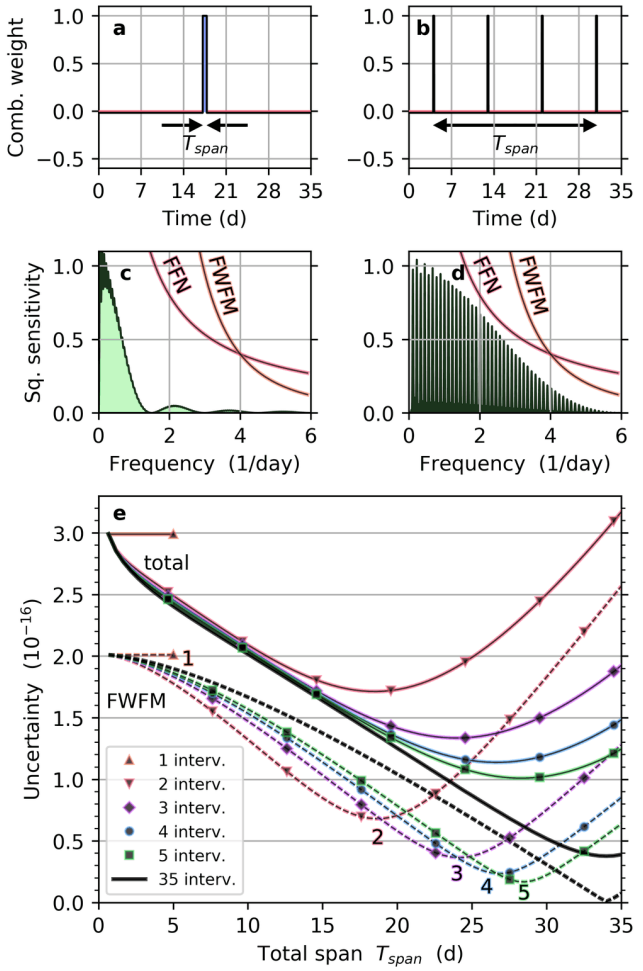

Fig. 4 Dead time uncertainty with distribution of measurements
(a) and **(b)** Maser frequency evaluation over a period of 35 d by identical total measurement times, either as a single interval (a) or equally distributed over 4 intervals (b), given in terms of the differential weighting function $g_\Delta(t)$, renormalized to 1. We describe the (identical) separation of the intervals by the span T_{span} from the beginning of the first interval to the end of the last. **(c)** and **(d)** Corresponding squared sensitivity function $|G_\Delta(f)|^2$ obtained by Fourier transform of $g_\Delta(t)$. Shortening the unobserved intervals (where $g_\Delta < 0$) causes the sensitivity to extend to higher Fourier frequencies (d), where both FFN and FWFM are of smaller magnitude (solid lines). **(e)** Overall stochastic uncertainty u_{stc} (solid lines) and contribution from u_{FWFM} (dashed lines) as a function of T_{span}. Colors and symbols indicate different numbers of intervals. Values represent an ensemble of $n_{\mathrm{HM}} = 3$, where four intervals are sufficient to reach $u_{\mathrm{stc}} = 1.14 \times 10^{-16}$. For any number of intervals, a suitable choice of T_{span} allows for $u_{\mathrm{FWFM}} \ll u_{\mathrm{stc}}$.

distributions of measurement time. This is shown in Fig.4. While a dense, even distribution throughout the evaluation period, e.g. daily measurements, yields the best results, this is not efficient when considering the effort required to initiate and maintain optical lattice clock operation. A division of the assumed 16 h measurement time discussed in Section **4** into four operating intervals of 4 h is sufficient to obtain $u_{\mathrm{stc}} = 1.1 \times 10^{-16}$ for a 35 d period. Here we take

advantage of the fact that the masers, carefully separated and isolated from environmental effects, show uncorrelated stochastic behavior. As demonstrated in Fig.2, the instability can then be reduced by averaging over multiple masers. Figure 4 is calculated for an ensemble of $n_{\mathrm{HM}} = 3$. For the measurement distribution in Fig.4(b):

$$u_{\mathrm{stc}}^2 = u_{\mathrm{FFN}}^2 + u_{\mathrm{FWFM}}^2 = \frac{(1.93 \times 10^{-16})^2}{n_{\mathrm{HM}}} + \frac{(5.93 \times 10^{-17})^2}{n_{\mathrm{HM}}} = (1.14 \times 10^{-17})^2 \quad (11)$$

This allows a comparison of the optical lattice clock to TAI with an overall uncertainty of

$$u_{\mathrm{TAI}}^2 = u_{l/\mathrm{Tai}}^2 + u_{\mathrm{sta}}^2 + u_{\mathrm{stc}}^2 = (2.0 \times 10^{-16})^2 + (1.4 \times 10^{-16})^2 + (1.1 \times 10^{-16}) = (2.7 \times 10^{-16})^2 \quad (12)$$

over 35 d. All these contributions are statistical in nature, allowing further reduction with repeated comparisons.

6 TAI calibrations

After seven qualifying measurements reported in Circular T 371 [22], NICT-Sr1 has contributed four measurements targeting TAI steering, with results reported in time for the monthly time scale evaluation performed by BIPM. These were included in Circular T 372-374 and 379. Their results are summarized in Table 1. Based on the measurements of the TAI scale interval d reported by all contributing frequency standards, a steering correction of 4×10^{-16} was applied to TAI over the period from December 2018 to May 2019.

For each of the data sets, all measurements of the maser frequency are collected on a fixed 10 s grid. We consider the observed $y_{\mathrm{HM}}(t)$ to represent a linear drift $y_{\mathrm{HM}}^{lin}(t) = m\,t + \bar{y}_{\mathrm{HM}}$ with overlaid stochastic frequency fluctuations $\delta y_{\mathrm{HM}}(t)$. We choose $t = 0$ to coincide with the midpoint of the evaluation period and define m and $\bar{y}_{\mathrm{HM}}$ to include any first order trend of the stochastic behavior.

The dead-time induced uncertainty u_{stc} discussed in the previous section then represents the error introduced in extracting $y_{\mathrm{HM}}^{lin}(t)$ from the available subset of data. This can be reduced by characterizing and compensating $\delta y_{\mathrm{HM}}(t)$: The DMTD system continuously provides frequency comparisons of all local maser frequencies. We select an ensemble of $n_{\mathrm{HM}} = 3$ to 5 well-behaved masers to form a reference frequency calculated at 1 h interval. After removing any first order trend, the interpolated difference of the characterized maser from the ensemble mean provides an approximation $\widetilde{\delta y}_{\mathrm{HM}}(t)$ of the stochastic fluctuations. We then calculate a linearized $\tilde{y}_{\mathrm{HM}}^{lin}(t) = y_{\mathrm{HM}}(t) - \widetilde{\delta y}_{\mathrm{HM}}(t)$ that is representative of the stability for the entire ensemble. Figure 2 demonstrates the resulting improvement: Where the original $y_{\mathrm{HM}}(t)$ (after subtracting a linear drift) shows the expected FFN-plateau near 2×10^{-16}, the corrected $\tilde{y}_{\mathrm{HM}}^{lin}(t)$ averages to below 1×10^{-16}, consistent with an improvement by $\sqrt{n_{\mathrm{HM}}}$ for an ensemble of $n_{\mathrm{HM}} = 5$ masers. Note that as defined, the correction has no effect on the extracted m and $\bar{y}_{\mathrm{HM}}$ when all of $y_{\mathrm{HM}}(t)$ is available.

We determine the statistical uncertainty by fitting the logarithm of the Allan variance, followed by extrapolation according to $\sigma_y^2(\tau) \propto 1/\tau$ up to the combined measurement time. For the exemplary data set, we find $u_{\mathrm{sta}} = \sigma_y(779\,853\ \mathrm{s}) = 3.9 \times 10^{-17}$. This represents the uncertainty of the mean over all observed data, with barycenter $t_0 \neq 0$. We correct for a maser drift $\delta_d = m\,t_0$ with an uncertainty $u_{\mathrm{drift}} = \sigma_m\,t_0$ according to the slope uncertainty σ_m determined by a linear fit. If the measurement intervals are suitably chosen, $t_0 \leq 1$ d, for which we find a typical uncertainty $u_{\mathrm{drift}} \leq 3 \times 10^{-17}$.

We consider an additional uncertainty from the microwave link between the maser and the frequency comb: While short-term phase excursions appear in the Allan deviation and are automatically included in the stability analysis, diurnal effects induced by e.g. temperature variations may affect multiple intermittent measurements in the same way and lead to a persistent frequency error. We in-

Table 1 Steering measurements of the TAI scale interval d by NICT-Sr1, reported in Circular T. All values are given in units of 10^{-15}. The statistical uncertainty u_A represents only the optical lattice clock. Uncertainties from maser instability (including dead time induced effects) are included in $u_{l/\mathrm{lab}}$. The operational duty cycle, size of the evaluated maser ensemble n_{HM} and the resulting u_{stc}, re-evaluated according to the methods described here, have been added for convenience.

Date	MJD period	d	u_A	u_B	$u_{l/\mathrm{lab}}$	$u_{l/\mathrm{Tai}}$	$\boldsymbol{u}$	u_{Srep}	duty	n_{HM}	u_{stc}
Dec. 2018	58454-58464	0.84	0.01	0.08	0.05	0.70	**0.71**	0.4	90.3%	5	0.006
Jan. 2019	58479-58509	0.90	0.04	0.08	0.32	0.23	**0.40**	0.4	1.4%	5	0.134
Feb. 2019	58514-58534	1.21	0.02	0.07	0.22	0.28	**0.37**	0.4	7.2%	4	0.186
June 2019	58644-58679	0.68	0.01	0.07	0.21	0.17	**0.28**	0.4	23.1%	3	0.202

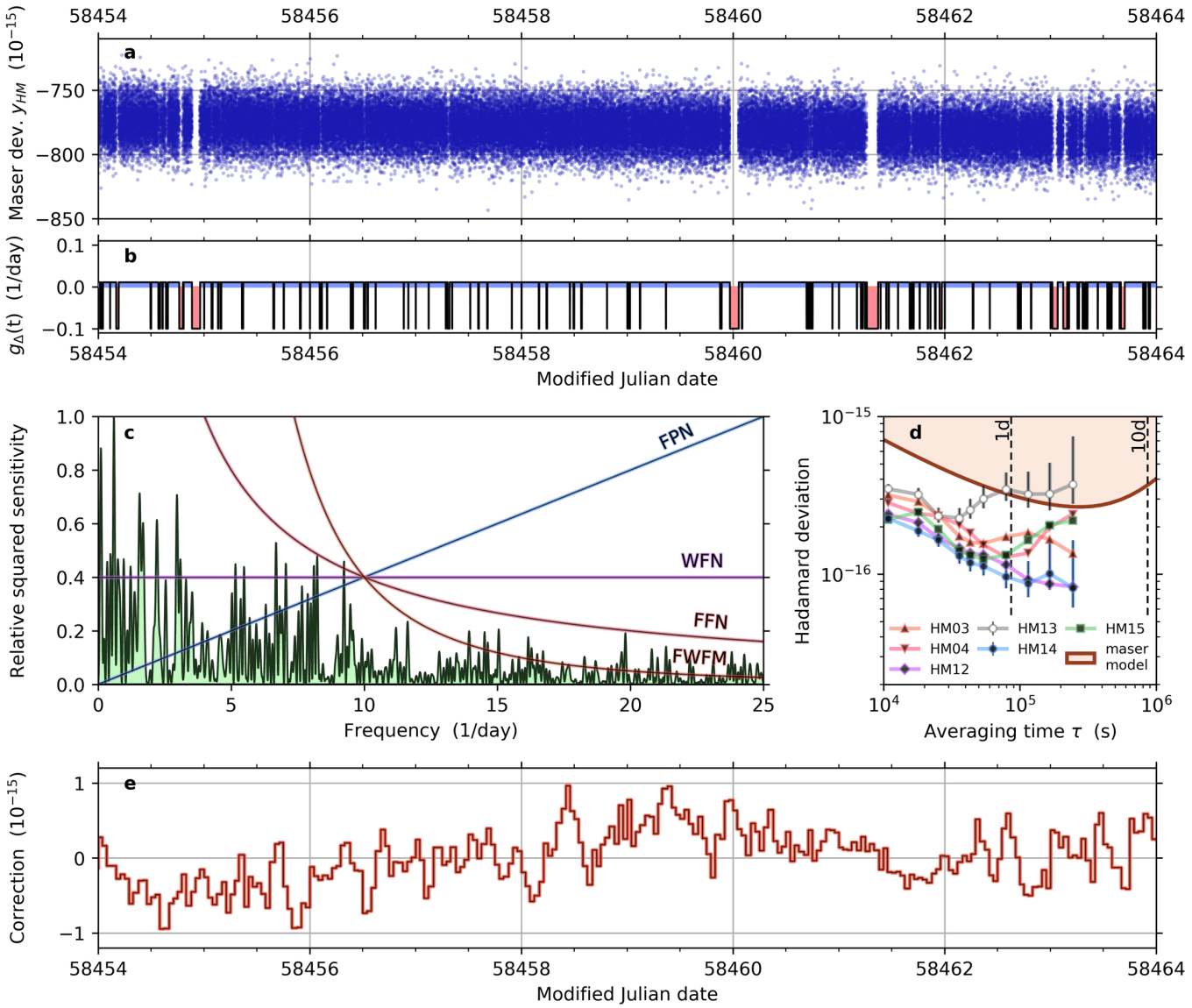

Fig. 5 **(a)** Available data for y_{HM} over the 10 d period of Fig.2 and **(b)** corresponding weighting function $g_\Delta(t)$
(c) Squared sensitivity function $|G_\Delta(f)|^2$ (green shaded graph) with overlaid curves representing the frequency dependence of the PSD for relevant noise types.
(d) The analysis applies the maser stability model (thick brown line) extracted from long-term DMTD data. Stable maser operation over the evaluation period is confirmed through the Hadamard deviation of the frequency difference of the individual masers from the selected ensemble (colored markers). HM JST#13 (open circles) has been excluded from the ensemble due to excess observed instability.
(e) Frequency corrections applied to reference maser HM JST#15 to compensate for deviation from linear drift, determined from the ensemble average.

vestigate this by binning the observed deviation from linear drift over the near-continuous $T = 10$ d data set according to the time of day. The results are consistent with a statistical distribution, and we find a residual deviation of $-1.98(7.70) \times 10^{-17}$ for the interval from 14:00 to 20:00 typical for intermittent measurements. For such measurements, we include this as a systematic type B uncertainty of $u^{\mathrm{typ}}_{B\_l/\mathrm{lab}} = \sqrt{-1.98^2 + 7.70^2} \times 10^{-17} = 7.95 \times 10^{-17}$.

For measurements of a significantly longer continuous measurement time T, we assume phase excursions of similar magnitude and assign a reduced uncertainty of $u^{\mathrm{typ}}_{B\_l/\mathrm{lab}}/(T/T_{\mathrm{ref}})$, where $T_{\mathrm{ref}} = 21\,600$ s is the length of the investigated 6 h reference period (Fig.6).

In the data reported in circular T, u_A and u_B directly represent the performance of the optical lattice clock All other uncertainties are included in

$$u_{l/\mathrm{lab}} = \sqrt{u^2_{\mathrm{sta}} + u^2_{\mathrm{drift}} + u^2_{\mathrm{stc}} + u^2_{B\_l/\mathrm{lab}}}. \quad (13)$$

7 Conclusion

In November 2018, NICT-Sr1 was approved as a sec-

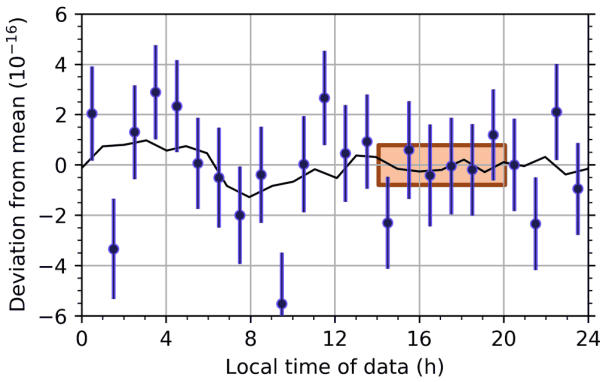

Fig. 6 Binning 10 d of data shows no statistically significant correlation of the frequency deviation with the time of day. Solid line shows a running mean over 6 hours. Orange shaded region indicates the interval where typical one-day measurements take place, to which we assign a systematic uncertainty of $u_{B\_l/\mathrm{lab}} = 7.95 \times 10^{-17}$.

ondary frequency standard by the Working Group on Primary and Secondary Frequency Standards (WG-PSFS), instituted by BIPM's Consultative Committee for Time and Frequency. The results of multiple calibration measurements of the international time scale TAI have since been published in Circular T. As shown in Fig.7, they are in good agreement with the reports of other standards.

By taking advantage of the inherent maser stability, intermittent clock operation allows monthly evaluations with statistical uncertainties of less than 3×10^{-16} (limited by the intercontinental link between NICT and BIPM) to be performed while only operating the optical lattice clock during four days. Although the contribution to the steering of TAI currently remains limited by the uncertainty $u_{\mathrm{Srep}} = 4 \times 10^{-16}$ assigned to ^{87}Sr as a secondary representation of the second, the calibration data may already be relevant whenever an insufficient number of primary frequency standards contribute.

The calibration data collected in the circular T can also be interpreted in the context of remote comparisons between the contributing standards [29], with TAI itself acting as a flywheel oscillator where measurement intervals are not completely aligned. Such an analysis has recently been used to determine the absolute frequency of a ^{171}Yb optical frequency standard to a fractional uncertainty of 2.1×10^{-16} [11]. Ongoing contributions by different secondary standards will rapidly accumulate such data and may prompt a re-evaluation of u_{Srep}.

In itself, reliable contribution of optical frequency standards to TAI is also an important milestone towards a new definition of the SI second [30], which may occur as early as 2030.

Appendix

Conversion between Hadamard variance and power spectral density

The Hadamard variance relates to the power spectral density $S_y(f)$ through [26]

$$\sigma_H^2(\tau) = \int_0^{f_h} S_y(f) \cdot |H(f)|^2 \, df, \tag{14}$$

where $|H(f)|^2 = \frac{16}{6}\left(\frac{\sin \pi \tau f}{\pi \tau f}\right)^2 \sin^4 \pi \tau f$ is the magnitude-squared transfer function after normalization according to the definition of the Hadamard variance. In the conventions of [27], this results in the conversion factors given in Table 2.

For a measurement with sampling interval τ_0, the cutoff frequency is typically considered to be $f_H \approx 1/(2\tau_0)$. The use of the Hadamard deviation makes it possible to include flicker-walk FM noise in the analysis, for which the Allan deviation does not converge. Here, $\gamma \approx 0.577$ is the Euler–Mascheroni constant.

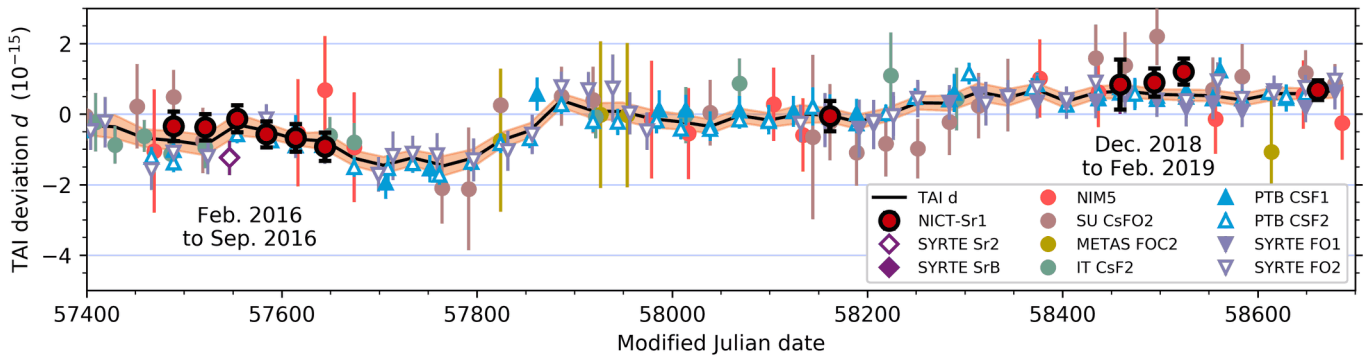

Fig. 7 Deviation d of TAI scale interval from the SI second
The measurements of NICT-Sr1 (red circles with heavy black outline) are in good agreement with the results of other primary and secondary standards (markers, as indicated) and the value of d reported in Circular T (black line, with orange shaded region indicating uncertainty). The indicated error bars for the secondary standards NICT-Sr1, SYRTE Sr2 and SYRTE SrB do not include u_{Srep}.

Table 2 Relation between power spectral density and Hadamard deviation

Noise Type	Abbrev.	$S_y(f)$	Hadamard (σ_H^2)
White phase noise	WPN	$h_2\, f^2$	$\frac{5\, f_H}{6\,\pi^2}\, h_2\, \tau^{-2} = \sigma_H^2(\tau)$
Flicker phase noise	FPN	$h_1\, f$	$\frac{10\,\gamma+\ln 48+10\ln(\pi\, f_H\, \tau)}{12\,\pi^2}\, h_1\, \tau^{-2} = \sigma_H^2(\tau)$
White frequency noise	WFN	h_0	$\frac{1}{2} h_0 \tau^{-1} = \sigma_H^2(\tau)$
Flicker frequency noise	FFN	$h_{-1}\, f^{-1}$	$\frac{1}{2}\ln\left(\frac{256}{27}\right) h_{-1} = \sigma_H^2(\tau)$
Random-walk freq. modulation	RWFM	$h_{-2}\, f^{-2}$	$\frac{1}{3}\pi^2 h_{-2}\, \tau = \sigma_H^2(\tau)$
Flicker-walk freq. modulation	FWFM	$h_{-3}\, f^{-3}$	$\frac{16}{6}\pi^2 \ln\left(\frac{3}{4}\cdot 3^{11/16}\right) h_{-3}\, \tau^2 = \sigma_H^2(\tau)$

References

1 E. F. Arias, G. Panfilo, and G. Petit, "Timescales at the BIPM," Metrologia 48, S145, 2011.
https://doi.org/10.1088/0026-1394/48/4/S04

2 T. P. Heavner, E. A. Donley, F. Levi, G. Costanzo, T. E. Parker, J. H. Shirley, N. Ashby, S. Barlow, and S. R. Jefferts, "First accuracy evaluation of NIST-F2," Metrologia 51, p.174, 2014.
https://doi.org/10.1088/0026-1394/51/3/174

3 F. Levi, D. Calonico, C. E. Calosso, A. Godone, S. Micalizio, and G. A. Costanzo, "Accuracy evaluation of ITCsF2: a nitrogen cooled caesium fountain," Metrologia 51, p.270, 2014.
https://doi.org/10.1088/0026-1394/51/3/270

4 M. Abgrall, B. Chupin, L. De Sarlo, J. Guéna, P. Laurent, Y. Le Coq, R. Le Targat, J. Lodewyck, M. Lours, P. Rosenbusch, G. D. Rovera, and S. Bize, "Atomic fountains and optical clocks at SYRTE: status and perspectives," C. R. Phys. 16, p.461, 2015.
https://doi.org/10.1016/j.crhy.2015.03.010

5 K Szymaniec, S. N. Lea, K. Gibble, S. E. Park, K. Liu, and P. Głowacki, "NPL Cs fountain frequency standards and the quest for the ultimate accuracy," J. Phys.: Conf. Ser. 723, 012003, 2016.
https://doi.org/10.1088/1742-6596/723/1/012003

6 S. Weyers, V. Gerginov, M. Kazda, J. Rahm, B. Lipphardt, G. Dobrev, and K. Gibble, "Advances in the accuracy, stability, and reliability of the PTB primary fountain clocks," Metrologia 55, p.789, 2018.
https://doi.org/10.1088/1681-7575/aae008

7 S. Falke, N. Lemke, C. Grebing, B. Lipphardt, S. Weyers, V. Gerginov, N. Huntemann, C. Hagemann, A. Al-Masoudi, S. Häfner, S. Vogt, U. Sterr, and C. Lisdat, "A strontium lattice clock with 3×10^{-17} inaccuracy and its frequency," New J. Phys. 16, 073023, 2014.
https://doi.org/10.1088/1367-2630/16/7/073023

8 J. Lodewyck, S. Bilicki, E. Bookjans, J.-L. Robyr, C. Shi, G. Vallet, R. Le Targat, D. Nicolodi, Y. Le Coq, J. and Guéna, "Optical to microwave clock frequency ratios with a nearly continuous strontium optical lattice clock," Metrologia 53, 1123, 2016.
https://doi.org/10.1088/0026-1394/53/4/1123

9 M. Pizzocaro, P. Thoumany, B. Rauf, F. Bregolin, G. Milani, C. Clivati, G. A. Costanzo, F. Levi, and D. Calonico, "Absolute frequency measurement of the $^1S_0$-$^3P_0$ transition of ^{171}Yb," Metrologia 54, p.102, 2017.
https://doi.org/10.1088/1681-7575/aa4e62

10 C. F. A. Baynham, R. M. Godun, J. M. Jones, S. A. King, P. B. R. Nisbet-Jones, F. Baynes, A. Rolland, P. E. G. Baird, K. Bongs, P. Gill, and H. S. Margolis, "Absolute frequency measurement of the $^2S_{1/2}$-$^2F_{7/2}$ optical clock transition in $^{171}Yb^+$ with an uncertainty of $4x10^{-16}$ using a frequency link to international atomic time," J. Mod. Opt. 65, pp.585-591, 2018.
https://doi.org/10.1080/09500340.2017.1384514

11 W. F. McGrew, X. Zhang, H. Leopardi, R. J. Fasano, D. Nicolodi, K. Beloy, J. Yao, J. A. Sherman, S. A. Schäffer, J. Savory, R. C. Brown, S. Römisch, C. W. Oates, T. E. Parker, T. M. Fortier, and A. D. Ludlow, "Towards adoption of an optical second: Verifying optical clocks at the SI Limit," arXiv:1811.05885, 2018.
https://arxiv.org/abs/1811.05885

12 S.M. Brewer, J.-S. Chen, A.M. Hankin, E.R. Clements, C.W. Chou, D.J. Wineland, D.B. Hume, and D.R. Leibrandt, "$^{27}Al^+$ quantum-logic clock with a systematic uncertainty below 10^{-18}," Phys. Rev. Lett. 123, 033201, 2019.
https://doi.org/10.1103/PhysRevLett.123.033201

13 C. Sanner, N. Huntemann, R. Lange, C. Tamm, E. Peik, M. S. Safronova, and S. G. Porsev, "Optical clock comparison for Lorentz symmetry testing," Nature 567, pp.204-208, 2019.
https://doi.org/10.1038/s41586-019-0972-2

14 M. Kramer, I. H. Stairs, R. N. Manchester, M. A. McLaughlin, A. G. Lyne, R. D. Ferdman, M. Burgay, D. R. Lorimer, A. Possenti, N. D'Amico, J. M. Sarkissian, G. B. Hobbs, J. E. Reynolds, P. C. C. Freire, and F. Camilo, "Tests of General Relativity from timing the double pulsar," Science 314, pp.97-102, 2006.
https://doi.org/10.1126/science.1132305

15 C. Grebing, A. Al-Masoudi, S. Dörscher, S. Häfner, V. Gerginov, S. Weyers, B. Lipphardt, F. Riehle, U. Sterr, and C. Lisdat, "Realization of a timescale with an accurate optical lattice clock," Optica 3, 563-569, 2016.
https://doi.org/10.1364/OPTICA.3.000563

16 H. Hachisu, F. Nakagawa, Y. Hanado, and T. Ido, "Months-long real-time generation of a time scale based on an optical clock," Scientific Reports 8, 4243, 2018.
https://doi.org/10.1038/s41598-018-22423-5

17 J. Yao, J. A. Sherman, T. Fortier, H. Leopardi, T. Parker, W. McGrew, X. Zhang, D. Nicolodi, R. Fasano, S. Schäffer, K. Beloy, J. Savory, S. Romisch, C. Oates, Scott Diddams, Andrew Ludlow, and Judah Levine, "Optical-clock-based time scale," arXiv:1902.06858, 2019.
https://arxiv.org/abs/1902.06858

18 W. R. Milner, J. M. Robinson, C. J. Kennedy, T. Bothwell, D. Kedar, D. G. Matei, T. Legero, U. Sterr, F. Riehle, H. Leopardi, T. M. Fortier, J. A. Sherman, J. Levine, J. Yao, J. Ye, and E. Oelker, "Demonstration of a time scale based on a stable optical carrier," arXiv:1907.03184, 2019.
https://arxiv.org/abs/1907.03184

19 Y. Hanado, K. Imamura, N. Kotake, F. Nakagawa, Y. Shimizu, R. Tabuchi, Y. Takahashi, M. Hosokawa, and T. Morikawa, "The new generation system of Japan Standard Time at NICT," Int. J. Navig. Obs. 2008, 841672, 2008.
http://doi.org/10.1155/2008/841672

20 F. Nakagawa, M. Imae, Y. Hanado, and M. Aida, "Development of multichannel dual-mixer time difference system to generate UTC (NICT)," IEEE Trans. Instr. Meas. 54, p.829, 2005.
https://doi.org/10.1109/TIM.2004.843382

21 G. Petit and Z. Jiang, "Precise Point Positioning for TAI computation," Int. J. Navig. Obs. 2008, 841672, 2008.
http://doi.org/10.1155/2008/562878

22 BIPM, "Circular T," available at https://www.bipm.org/jsp/en/TimeFtp.jsp

23 G. Panfilo and T. E. Parker, “A theoretical and experimental analysis of frequency transfer uncertainty, including frequency transfer into TAI,” Metrologia 47, pp.552-560, 2010.
https://doi.org/10.1088/0026-1394/47/5/005

24 H. Hachisu and T. Ido, “Intermittent optical frequency measurements to reduce the dead time uncertainty of frequency link,” Jpn. J. Appl. Phys. 54, 112401, 2015.
https://doi.org/10.7567/JJAP.54.112401

25 BIPM, “Recommended values of standard frequencies for applications including the practical realization of the metre and secondary representations of the definition of the second (2017),” available at http://www.bipm.org/en/publications/mises-en-pratique/standard-frequencies.html

26 W. J. Riley, “Handbook of frequency stability analysis,” Natl. Inst. Stand. Technol. Spec. Publ. 1065, 2008.
https://www.nist.gov/publications/handbook-frequency-stability-analysis

27 S.T. Dawkins, J. J. McFerran, and A. Luiten, “Considerations on the measurement of the stability of oscillators with frequency counters,” IEEE Trans. UFFC 54, pp.918-925, 2006.
https://doi.org/10.1109/TUFFC.2007.337

28 N. J. Kasdin and T. Walter, “Discrete simulation of power law noise (for oscillator stability evaluation),” Proc. 1992 IEEE Freq. Contr. Symp. (Hershey, PA, USA), pp.274-283, 1992.
https://doi.org/10.1109/FREQ.1992.270003

29 H. Hachisu, G. Petit, F. Nakagawa, Y. Hanado, and Tetsuya Ido, “SI-traceable measurement of an optical frequency at the low 10^{-16} level without a local primary standard,” Opt. Express 25, 8511, 2017.
https://doi.org/10.1364/OE.25.008511

30 F.Riehle, P. Gill, F. Arias, and L. Robertsson, “The CIPM list of recommended frequency standard values: guidelines and procedures,” Metrologia 55, p.188, 2018.
https://doi.org/10.1088/1681-7575/aaa302

伊東宏之　（いとう　ひろゆき）
総務省
国際戦略局
技術政策課
技術企画調整官
博士（理学）
周波数標準、レーザー分光

後藤忠広　（ごとう　ただひろ）
電磁波研究所
時空標準研究室
主任研究員
博士（工学）
時刻比較、精密軌道決定

井戸哲也　（いど　てつや）
電磁波研究所
時空標準研究室
室長
博士（工学）
光周波数標準、光周波数計測

Nils Nemitz　（にるす　ねみっつ）
電磁波研究所
時空標準研究室
主任研究員
Dr. rer. nat.
光周波数コム、光周波数標準、標準時

蜂須英和　（はちす　ひでかず）
電磁波研究所
時空標準研究室
主任研究員
博士（工学）
光周波数標準、光格子時計とその応用

中川史丸　（なかがわ　ふみまる）
電磁波研究所
時空標準研究室
主任研究員
博士（理学）
時間周波数標準、時刻比較